The Journal of Physiology



# Interactions between calcium-induced arrhythmia triggers and the electrophysiological–anatomical substrate underlying the induction of atrial fibrillation

Michael A. Colman[1], Marta Varela[2,3], Rob S. MacLeod[4], Jules C. Hancox[5] and Oleg V. Aslanidi[3]

[1]*School of Biomedical Sciences, Faculty of Biological Sciences, University of Leeds, Leeds, UK*
[2]*National Heart & Lung Institute, Faculty of Medicine, Imperial College London, London, UK*
[3]*School of Biomedical Engineering & Imaging Sciences, King's College London, London, UK*
[4]*The Scientific Computing and Imaging Institute, University of Utah, Salt Lake City, UT, USA*
[5]*School of Physiology, Pharmacology & Neuroscience, Faculty of Life Sciences, University of Bristol, Bristol, UK*

Handling Editors: Natalia Trayanova & T Alexander Quinn

The peer review history is available in the Supporting Information section of this article (https://doi.org/10.1113/JP285740#support-information-section).

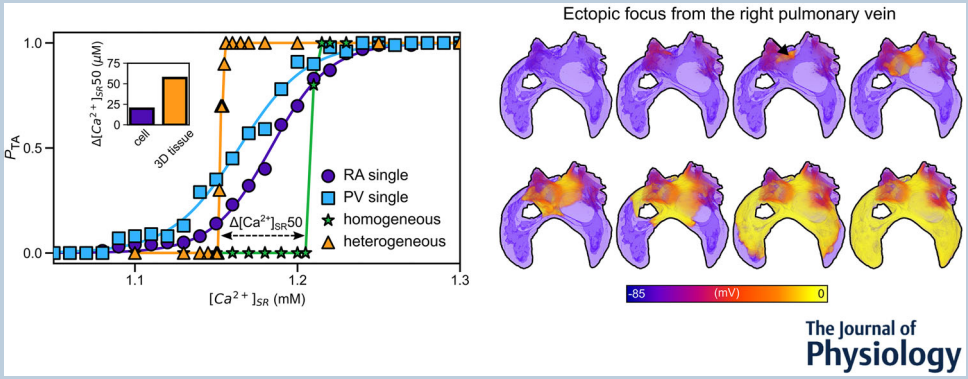


**Abstract** Atrial fibrillation (AF) is the most common cardiac arrhythmia and is sustained by spontaneous focal excitations and re-entry. Spontaneous electrical firing in the pulmonary vein (PV) sleeves is implicated in AF generation. The aim of this simulation study was to identify the mechanisms determining the localisation of AF triggers in the PVs and their contribution to the genesis of AF. A novel biophysical model of the canine atria was used that integrates stochastic, spontaneous subcellular $Ca^{2+}$ release events (SCRE) with regional electrophysiological heterogeneity in ionic properties and a detailed three-dimensional model of atrial anatomy, micro-architecture and patchy fibrosis. Simulations highlighted the importance of the smaller inward rectifier potassium current ($I_{K1}$) in PV cells compared to the surrounding atria, which enabled SCRE more readily to result in delayed-afterdepolarisations that induced triggered activity. There was a leftward shift in the dependence of the probability of triggered activity on sarcoplasmic reticulum $Ca^{2+}$ load. This feature was accentuated in 3D tissue compared to single cells (Δ half-maximal

**Michael Colman** received his Masters in Theoretical Physics from the University of Manchester in 2008, which was followed by a PhD in Biological Physics in 2012. Now at the University of Leeds, his research interests are in the development and application of novel multi-scale joint experimental–simulation frameworks to understand the mechanisms of cardiac electrophysiology and intracellular calcium handling, with the aim to improve understanding of cardiac dysfunction and ultimately lead to better diagnosis and treatment strategies. He has a primary focus on the multi-scale interactions of components from the sub-micron to the whole-heart scale, and the role of these interactions in the pathologies associated with heart failure, atrial fibrillation, and ageing.

 DOI: 10.1113/JP285740

$[Ca^{2+}]_{SR} = 58\ \mu M$ *vs.* $22\ \mu M$). In 3D atria incorporating electrical heterogeneity, excitations preferentially emerged from the PV region. These triggered focal excitations resulted in transient re-entry in the left atrium. Addition of fibrotic patches promoted localised emergence of focal excitations and wavebreaks that had a more substantial impact on generating AF-like patterns than the PVs. Thus, a reduced $I_{K1}$, less negative resting membrane potential, and fibrosis-induced changes of the electrotonic load all contribute to the emergence of complex excitation patterns from spontaneous focal triggers.

(Received 28 September 2023; accepted after revision 17 January 2024; first published online 19 February 2024)
**Corresponding author** M. A. Colman: School of Biomedical Sciences, Faculty of Biological Sciences, University of Leeds, Leeds, UK. Email: m.a.colman@leeds.ac.uk

**Abstract figure legend** Left: probability of cellular trigger activity or tissue focal excitation ($P_{TA}$) as a function of sarcoplasmic reticulum load ($[Ca^{2+}]_{SR}$) in isolated cells from the right atrium (RA) and pulmonary veins (PV) and in homogeneous (all cells are modelled as RA) and heterogeneous 3D tissue models. The cellular differences are enhanced in 3D, leading to a large shift in the half-maximal $[Ca^{2+}]_{SR}$ observed ($\Delta[Ca^{2+}]_{SR}50$). Right: temporal snapshots showing the membrane potential ($V_m$) in the 3D atria, corresponding to a focal excitation originating from the right pulmonary vein.

**Key points**

- Focal excitations in the atria are most commonly associated with the pulmonary veins, but the mechanisms for this localisation are yet to be elucidated.
- We applied a multi-scale computational modelling approach to elucidate the mechanisms underlying such localisations.
- Myocytes in the pulmonary vein region of the atria have a less negative resting membrane potential and reduced time-independent potassium current; we demonstrate that both of these factors promote triggered activity in single cells and tissues.
- The less negative resting membrane potential also contributes to heterogeneous inactivation of the fast sodium current, which can enable re-entrant-like excitation patterns to emerge without traditional conduction block.

## Introduction

Atrial fibrillation (AF) is the most common cardiac arrhythmia, imposing a huge healthcare burden (Burdett & Lip, 2022; Camm et al., 2010; Stewart et al., 2004). AF is characterised by rapid and irregular electrical activity in the atria, which can be underlain by multiple structural, electrical and neurohormonal dysfunction at the cellular and tissue scale. AF triggers are commonly associated with the pulmonary vein (PV) sleeve region of the left atrium, where abnormal intracellular $Ca^{2+}$ events and neurohormonal dysregulation may lead to spontaneous electrical firing. Triggered ectopic electrical waves ('focal excitations') may break down to generate further sustained wave sources: re-entrant drivers ('rotors'). Substrates for re-entry and AF generation include changes of the electrical excitation wavelength, proliferation of fibrosis and complex arrangement of fibres in atrial tissue (Nattel et al., 2014). Once established, AF induces mechanisms for self-perpetuation ('AF begets AF'), with further structural, electrical and innervation remodelling superimposed upon pre-existing pathologies to produce more persistent and recurrent AF (Nattel et al., 2014; Schotten et al., 2011). The diversity of underlying factors hampers the dissection of their relative roles in the complex mechanisms of AF progression, and hence the development of more effective treatments.

Biophysical modelling of the heart provides a quantitative framework for integrating diverse cell-to-organ data and for dissecting arrhythmogenic behaviours that emerge from the complex interactions of multiple underlying factors (Colman et al., 2022; Dössel et al., 2021; Heijman et al., 2021; Lopez-Perez et al., 2015; Niederer et al., 2019; Vagos et al., 2018). Such an integrative approach is extremely difficult to implement in a purely experimental or clinical setting. Computational models of the atria have provided important insights into various mechanisms of AF, from cellular events to re-entry in atrial tissues and various aspects of remodelling in the entire 3D atria (Aslanidi et al., 2011; Cherry et al., 2007;

Colman et al., 2013; Dössel et al., 2012; Roney et al., 2018). For example, detailed 3D biophysical models of the atria have shown that tissue anisotropy and electrical heterogeneity can lead to conduction blocks and the initiation of re-entry, whereas AF-induced remodelling decreases the wavelength and facilitates the sustenance of re-entrant waves (Colman et al., 2014; Greene et al., 2022; Morgan et al., 2016; Varela et al., 2016).

Triggers for the initial ectopic electrical waves, governing the spontaneous transition from sinus rhythm to an AF event, are significantly less studied (de Bakker et al., 2002). They have been linked with the PV sleeves (Haïssaguerre et al., 1998; Sanders et al., 2005), but the underlying mechanisms of such triggers are incompletely understood. Paroxysmal AF can result in an increased $Ca^{2+}$ transient amplitude without major changes in atrial action potential duration (APD) in atrial cells (Grandi et al., 2011; Voigt et al., 2014; Workman, 2010). Enhanced ryanodine receptor (RyR) sensitivity can also lead to abnormal diastolic $Ca^{2+}$ release, and subsequent $Ca^{2+}$ extrusion from the cell via the sodium–calcium exchanger current ($I_{NaCa}$), leading to cellular delayed after-depolarisations (DADs). If of sufficient magnitude to reach the threshold for activation of the fast sodium current ($I_{Na}$), these DADs can elicit full triggered action potentials (triggered activity, TA) in single cells, which have the potential to induce focal excitations in tissue. Indeed, experiments show that enhanced diastolic $I_{NaCa}$ following rapid pacing can link spontaneous $Ca^{2+}$ transients with ectopic electrical activity (Henry et al., 2018; Patterson et al., 2005, 2006; Shiferaw et al., 2017), including in the PVs specifically (Namekata et al., 2009). However, $Ca^{2+}$ handling dynamics in atrial cells is not well characterised, and detailed information on heterogeneity in $Ca^{2+}$ handling between different regions of the atria is limited in large animal models and humans.

Several characteristics of the atrial PV sleeves have been linked to arrhythmia mechanisms. We and other groups have previously shown that the APD gradient between the PV and LA region can promote unidirectional conduction block (Aslanidi et al., 2012; Colman et al., 2013; Roney et al., 2018). Combined with the anatomical openings of the vein themselves, this can promote the development of transient or sustained re-entry (Aslanidi, Colman, et al., 2013; Cherry et al., 2007; Colman et al., 2014; Varela et al., 2016). Moreover, the PVs generally display a less negative resting membrane potential (RMP) than the surrounding atria (Ehrlich et al., 2003; Jæger et al., 2022; Mahida et al., 2015; Namekata et al., 2009; Takahara et al., 2014), which may substantially promote triggered activity: recent studies have shown a highly sensitive dependence of the magnitude of DADs and probability of TA on the inwardly rectifying potassium current ($I_{K1}$) and RMP (Campos et al., 2015; Colman, 2019). Some studies have further revealed a higher propensity for spontaneous $Ca^{2+}$ release events (SCRE), DADs and also early after-depolarisations (EADs) in PV cells compared to the atria (Bond et al., 2020; Rietdorf et al., 2014).

The PV region is also associated with high levels of fibrosis, which can potentially promote focal excitations through reducing inter-myocyte electrotonic interactions. Previous studies have also shown that dimensionality is a strong controller of focal excitations: they are easier to induce in 1D strands than 2D slices, and in 2D slices compared to 3D slabs (Campos et al., 2015; Colman, 2019; Xie et al., 2010). Therefore, anatomical features that may affect electrotonic interactions, such as anisotropy, fibrosis and wall thickness, may all contribute to the development of focal excitations.

The aim of this study was to evaluate the impact of these multiple factors on the development of focal excitations *in silico*, while controlling for the dynamics of SCRE. The hypotheses underpinning the study are that (1) the less hyperpolarised RMP and reduced $I_{K1}$ in the PV region preferentially locates focal excitations, and (2) fibrosis promotes focal excitations and simultaneously provides the substrate for them to generate transient or sustained arrhythmia.

## Methods

The overall approach of this study was to control for the properties of SCRE dynamics (i.e. to control the timing and magnitude of events) and assess the interaction of these trigger events with the differing cellular and anatomical contexts in various regions of the atria. To achieve this, we combined our previously developed models of canine 3D atrial anatomy and heterogeneous cell and tissue electrophysiology (Varela et al., 2016) with models of spatial subcellular calcium handling and a reduced model of SCRE (Colman, 2019).

### Single cell models of heterogeneous canine atrial electrophysiology

We updated our previously developed family of heterogeneous canine atrial cell models (Varela et al., 2016), which includes a distinct electrophysiological description of four regions corresponding to the right atrium (RA), left atrium (LA), crista terminalis–Bachman's bundle (CT-BB) and PVs (Fig. 1*Aa*). The primary difference between the four model variants is in the magnitude and formulation of key ion currents, including the L-type calcium current ($I_{CaL}$) and $I_{K1}$ (Varela et al., 2016). The CT and BB were considered to have the same electrophysiology, as in the previous study (Varela et al., 2016), because they shared similar conductive bundle features distinct from the surrounding atria, with only small electrophysiological differences

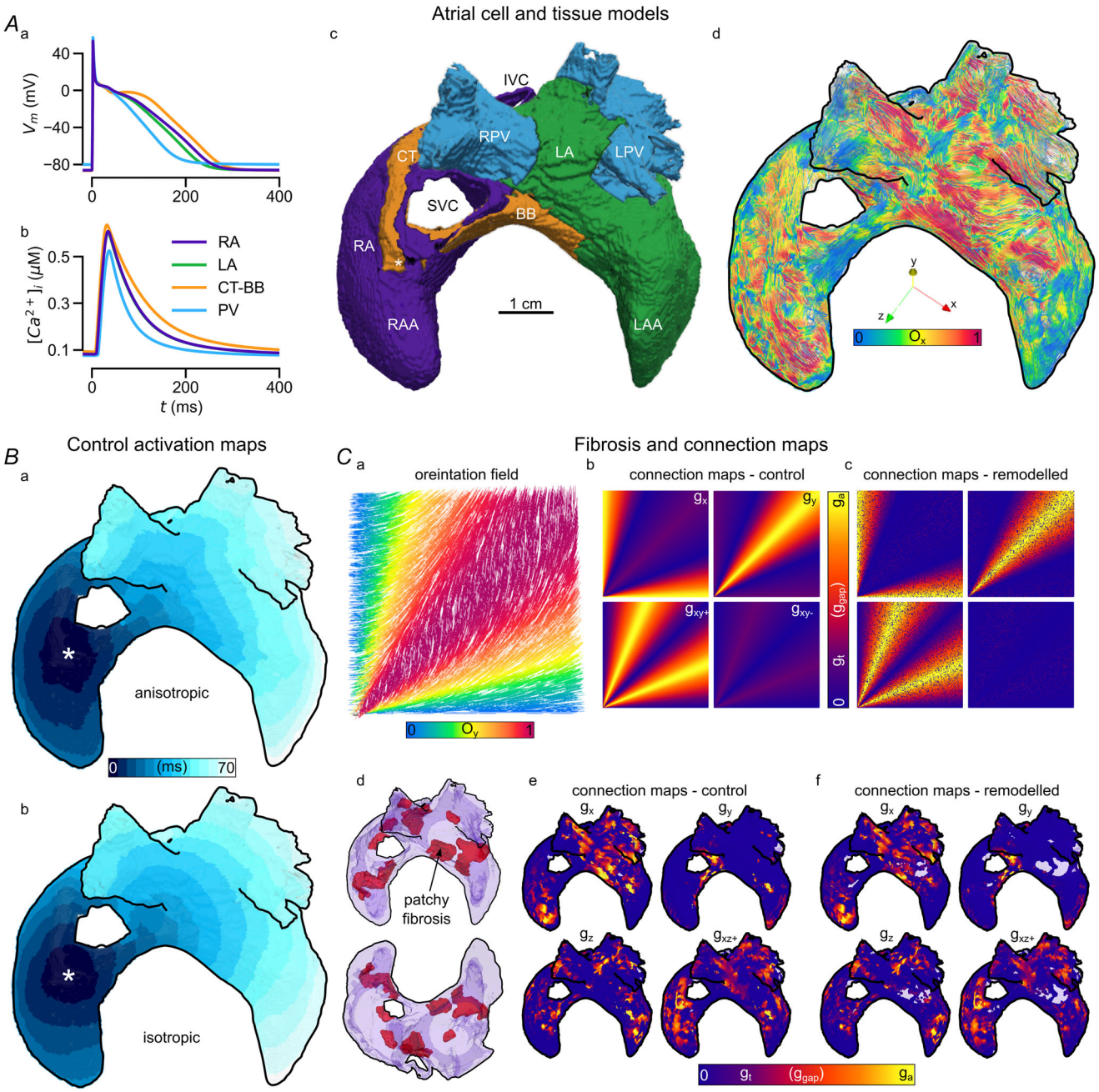


**Figure 1. Canine atrial cell and tissue models**
*A*, action potentials (*a*) and intracellular $Ca^{2+}$ transients (*b*) produced by the integrated canine atrial cell models for the four distinct regions of the right and left atrium (RA, blue, and LA, green, respectively), crista-terminalis–Bachmann's bundle (CT-BB, yellow) and the pulmonary vein sleeves (PV, orange). *c*, labelled illustration of the segmented 3D canine atrial geometry, with unsegmented anatomical features labelled for clarity (e.g. right and left atrial appendages, RAA, LAA, and the superior and inferior vena cava, SVC and IVC). *d*, illustration of the myocyte orientation field from the same anatomical orientation. The colour scale indicates the magnitude of the *x*-component of the orientation. *B*, activation patterns in the control model in anisotropic (*a*) and isotropic (*b*) conditions. Asterisk indicates sinus rhythm pacing site, approximately at the location of the SAN. *C*, illustration of the 2D anisotropic tissue model (*a*) and the connection maps associated with control (*b*) and fibrosis/remodelled (*c*), further to the fibrosis patches in 3D (*d*) and the associated connection maps in control (*e*) and remodelled (*f*). Connection maps show the magnitude of the connections between adjacent nodes in each of the four directions (2D) and four selected directions (3D). See Supporting information, Text S2 for further details. [Colour figure can be viewed at wileyonlinelibrary.com]

observed between the two bundles (Burashnikov et al., 2004; Feng et al., 1998). These ion current models were then combined with our previously presented reduced $Ca^{2+}$ handling model (Colman, 2019) that has been designed to be suitable for integration with multi-scale methods to describe stochastic spontaneous $Ca^{2+}$ release (see details in 'Spontaneous calcium release events' below). Thus, all of the intracellular $Ca^{2+}$ handling equations in the original Varela et al. (2016) model were replaced with those from the Colman (2019) model, and the formulations of $Ca^{2+}$ currents (e.g. $I_{CaL}$, $I_{NaCa}$) were updated accordingly (Supporting information, Text S1). The PV model was further modified to capture the large difference in RMP observed between PVs and surrounding atria (Ehrlich et al., 2003; Takahara et al., 2014), by shifting the reversal potential of $I_{K1}$ by 9 mV (Supporting information, Text S1). The four updated model variants display distinct action potential and $Ca^{2+}$ transient morphology (Fig. 1*Aa*, *b*), reflecting the atrial heterogeneity observed in cellular experiments (Ehrlich et al., 2003).

To induce $Ca^{2+}$ overload in the sarcoplasmic reticulum (SR), which is known to promote SCRE (Eisner et al., 2009, 2013; Landstrom et al., 2017; Nattel & Dobrev, 2012; Voigt et al., 2014), a simplified model of sympathetic regulation of atrial cells was implemented. This model was parameterised to increase $Ca^{2+}$ influx to load the SR while maintaining a similar APD to control, through an increase in the current densities/maximal flux rates (Heijman et al., 2011; Workman, 2010) of $I_{CaL}$, the SR $Ca^{2+}$ uptake pump ($J_{up}$), and the potassium channels $I_{Kur}$ and $I_{Ks}$ (Supporting information, Text S1).

## Control 2D tissue and 3D atrial models

Idealised tissue models were implemented as isotropic homogeneous 2D tissue slices with every node assigned to a single cell type (each of the four different regions). These 2D models were used to study the parameters that promote the development of focal excitations under various conditions (see 'Simulation protocols' below). Regional cell models were then mapped onto broadly segmented regions of a previously reconstructed 3D model of the canine atria which includes realistic image-derived myofibre orientations (Aslanidi, Nikolaidou, et al., 2013; Varela et al., 2016). Briefly, atrial geometry was reconstructed from contrast-enhanced micro-computed tomography images, with the enhancement enabling local myocyte orientation to be estimated. Thus, the model contains representations of the anatomy of the atria, including local myocyte orientation, with different regions segmented to reflect the different cell models available, i.e. RA, LA, CT-BB and PVs (Fig. 1*Ac*). Control pacing was induced by applying a stimulus to the sino-atrial node (SAN) region of the right atrium (Fig. 1*Ac*). In order to assess the influence of myocyte orientation-related anisotropy, an isotropic model was also implemented, in which the total activation time of the atria was matched (parameters in Supporting information, Text S1) to the anisotropic model to facilitate like-for-like comparisons (Fig. 1*B*).

Action potential propagation was modelled by solving the monodomain equation using the finite differences method (FDM). The model was solved with a spatial integration step, $\Delta x = 0.3$ mm, a temporal integration step, $\Delta t = 0.01$ ms, and diffusion conductivity parameters $D_{longitudinal} = 0.4$ mm$^2$/ms and $D_{transverse} = 0.04$ mm$^2$/ms (for the anisotropic models) and $D_{global} = 0.25$ mm$^2$/ms (for isotropic simulations). This resulted in conduction velocities of 0.962 m/s and 0.213 m/s parallel and transverse to the local myocyte orientation, respectively, in the RA model, consistent with experimental recordings (Anyukhovsky et al., 2002; Guerra et al., 2006; Li et al., 1999) and the previous, inherited model (Varela et al., 2016).

## Remodelled 2D and 3D atrial models with fibrosis

Patchy fibrosis was implemented according to our recently proposed method: axial (longitudinal) and transverse intercellular connections were differentially removed in regions of fibrosis, representing its insulating impact (de Jong et al., 2011). This cannot be directly implemented using the FDM approach, and thus our recently proposed network model (Colman & Benson, 2023) was used for all fibrosis simulations. Briefly, this model involves creating a network of axial and transverse connections between nodes (derived from the local myocyte orientation), which can later be selected for removal to simulate fibrosis (see the original study for more details). In 2D, there are eight directions in which nodes can be coupled, which reduces to four when accounting for symmetry arguments (Fig. 1*Cb*): the *x*-direction ($g_x$), the *y*-direction ($g_y$), the diagonal where the sign on *x* and *y* is the same ($g_{xy+}$) and the diagonal where the sign on *x* and *y* is opposite ($g_{xy-}$). See Supporting information, Text S2 for further details of the construction of this approach. The model reduces to the same as FDM in idealised cases (fibre orientation pointing directly along an axis) which enables comparable parameters to be used for both FDM and network model simulations (Supporting information, Text S2).

For 2D simulations, a spatially varying vector field was used to define local myocyte orientation (Fig. 1*Ca*). Control simulations were performed with full connections retained. Fibrosis was implemented by randomly removing 80% of transverse and 20% of axial cellular connections throughout the whole of the tissue (Fig. 1*Cb*, *c*), representing the preferential loss of

connections transverse to fibre bundle orientation (de Jong et al., 2011).

Patchy fibrosis in the 3D atria was assigned to regions based on previously performed amplitude analysis of electroanatomical mapping (EAM) data from canine atria (Fig. 1*Cd*). Briefly, a neurostimulator (InterStim, Medtronic Inc., Minneapolis, Minnesota, USA) was implanted in a mongrel dog (∼25 kg) and chronic AF was induced with rapid atrial pacing (RAP) (Yamashita et al., 2019). Persistent AF was defined as maintaining AF for longer than 20 min following the removal of stimulation. EAMs were acquired during sinus rhythm with CARTO (Biosense Webster, Diamond Bar, CA, USA) using a non-irrigated 3.5-mm-tip NaviStar (Biosense Webster) catheter. Bipolar electrograms were acquired in the LA with a high-pass filter of 30 Hz and a low-pass filter of 400 Hz. The amplitude of these signals was interpolated on the dog's atrial mesh using bicubic interpolation. Regions with an amplitude below 0.5mV were labelled as fibrosis (Jadidi et al., 2016). The fibrosis maps were registered to the segmented atrial canine model (Varela et al., 2016) using landmark alignment followed by affine registration implemented using Image Registration Toolkit (IRTK) (Varela et al., 2017). Axial and transverse connections within the fibrotic patch regions were then removed according to the same thresholds as in the 2D simulations, resulting in heterogeneous connection maps (Fig. 1*Ce*, *f*).

## Spontaneous calcium release events

Spontaneous $Ca^{2+}$ sparks and waves manifest at the whole-cell level as transient activity of the RyRs, which can trigger depolarisations of the membrane potential (Fig. 2*A*). Modelling spatially resolved $Ca^{2+}$ spark events at the whole-cell scale is computationally costly, and therefore infeasible for whole-organ simulations requiring hundreds of thousands or millions of cell models. We therefore implemented a phenomenological model that captures these dynamics at substantially reduced cost through approximating the RyR waveforms associated with whole-cell SCRE (Colman, 2019). We define spontaneous release functions (SRF) that describe the whole-cell RyR transient activity across the range of behaviours, from slowly propagating, low-magnitude $Ca^{2+}$ waves through to almost synchronous whole-cell release (Fig. 2*Ba*). SRFs are defined by two primary controllable parameters: the duration (λ, which inversely correlates with the magnitude, as approximately the same total amount of $Ca^{2+}$ is released during whole-cell events) and the initiation (or latency) time, $t_i$. To implement these SRF, the proportion of open RyRs in the cell model can be clamped to this waveform, allowing the $Ca^{2+}$ concentrations and $Ca^{2+}$-dependent currents to respond in the same way that they would during SCRE in a detailed cell model. Thus, SCRE at different timing and magnitudes can be controllably induced in efficient, non-spatial cell models (Fig. 2*Bb*).

To capture the stochastic nature of SCRE (i.e. the inherent randomness in the timing and magnitude of events), the SRF parameters (λ, $t_i$) can be independently randomly sampled from defined distributions (Fig. 2*Bc*). Thus, we can define the statistics of SCRE and then impose these properties in tissue models to study emergent behaviour. The distributions that give the statistics of each parameter can be described by two parameters each: the centre and width of the distributions. Dynamic dependence on the $[Ca^{2+}]_{SR}$ load can be implemented by defining these four distribution parameters as functions of the junctional $[Ca^{2+}]_{SR}$ (Fig. 2*Bd*). The model employs an algorithm wherein, upon relaxation, the junctional $[Ca^{2+}]_{SR}$ is used to calculate the SRF distribution parameters, from which SRF waveform parameters are randomly sampled. On subsequent time steps, the algorithm checks whether the $[Ca^{2+}]_{SR}$ has changed by more than a set threshold (>0.01 mM) since the SRF were previously set. If it has changed by more than this amount (but the SRF has not yet been initiated), then the parameters are recalculated based on this new $[Ca^{2+}]_{SR}$ (Colman, 2019).

The impact of SCRE can therefore be assessed at a constant $[Ca^{2+}]_{SR}$ against specific distribution parameters (separating synchronisation and magnitude considerations) or against varying $[Ca^{2+}]_{SR}$ load (where both synchronisation and magnitude vary together according to the $[Ca^{2+}]_{SR}$ input). This approach enables independent cellular SCRE to be simulated in coupled tissue models and the impact on membrane potential studied (Fig. 2*C*).

## Simulation protocols

At both cellular and tissue levels, for studies correlating the probability of TA ($P_{TA}$) with $[Ca^{2+}]_{SR}$, all cell models were pre-paced at a cycle length of 400 ms with the sympathetic regulation model implemented to promote $[Ca^{2+}]_{SR}$ loading. The exact desired $[Ca^{2+}]_{SR}$ load (the control variable) was set at a time just before the earliest possible SCRE, in order to ensure any concentration drift was avoided and that all data were being compared at the $[Ca^{2+}]_{SR}$ levels intended. The same process was followed in idealised 2D tissue and in 3D atrial models, where the model was run either with heterogeneous cell models associated with each region, or with the whole tissue described by the RA cell model (homogeneous model). The $P_{TA}$ was simply given as the proportion of simulations that did induce TA at each $[Ca^{2+}]_{SR}$. TA was considered to be when the membrane potential, $V_m$, associated with SCRE reached above a threshold of −25 mV, below which deflections were considered as DADs.

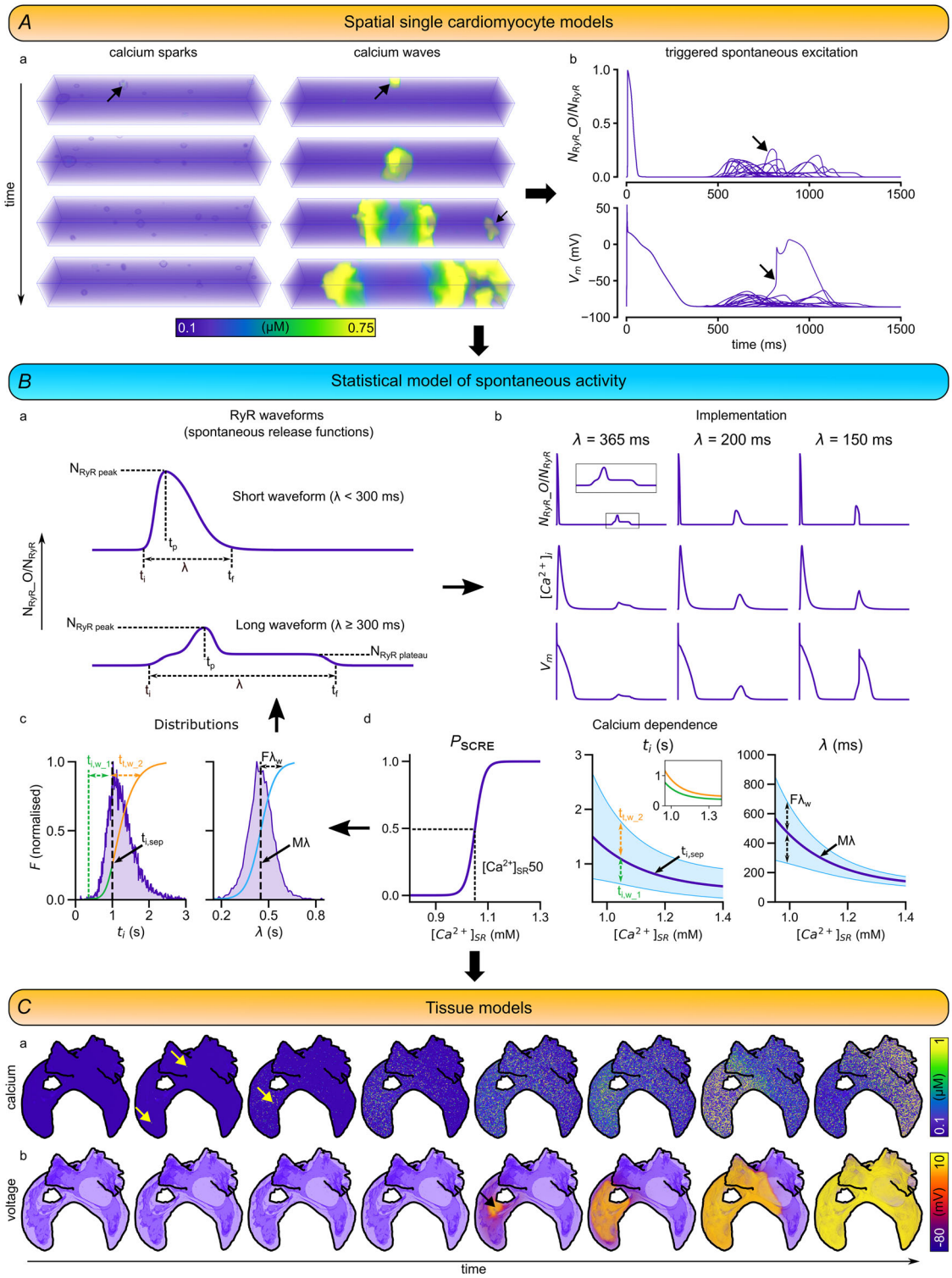


**Figure 2. Illustration of the spontaneous release functions**
*A*, illustration of $Ca^{2+}$ sparks and waves in a spatially detailed model of the cell and the resulting RyR transient (the proportion of open RyRs at each time point) and $V_m$ dynamics. *Ba*, example spontaneous release function waveforms, describing the proportion of open RyR during spontaneous $Ca^{2+}$ release, illustrating both short (upper) and long (lower) waveforms. Labelled parameters are the initiation time, $t_i$, time of the peak, $t_p$, duration, λ, and final time, $t_f$, the peak of the waveform ($N_{RyR\_peak}$), and the plateau value, $N_{RyR\_plateau}$. *b*, illustration of the implementation of waveforms at three different durations (λ), integrated with the non-spatial electrophysiological model. Note that amplitude of the proportion of RyRs is inversely proportional to λ, corresponding to the same

total release of $Ca^{2+}$. It can be seen that the RyR waveform underlies a $Ca^{2+}$ transient, which interacts with the AP. *c*, illustration of the distributions from which the waveform parameters, $t_i$ and λ, are sampled (the remaining waveform parameters are derived from these). These distributions are defined by key parameters: $t_{i\_sep}$, $t_{i\_w1}$, and $t_{i\_w2}$; median duration, $M\lambda$, and width of the duration distribution, $F\lambda_w$. *d*, functions which determine the distribution parameters from SR calcium concentration. The $[Ca^{2+}]_{SR}50$ corresponds to the $[Ca^{2+}]_{SR}$ load at which probability of a spontaneous release, $P_{SCRE}$, is 50%. *C*, illustration of the effect of SRF implemented in the 3D atrial model, demonstrating how independent cellular SCRE (*a*) can lead to focal excitations (*b*). Yellow arrows point to large local cellular SCRE occurring within the tissue. [Colour figure can be viewed at wileyonlinelibrary.com]

In single cells, for studies correlating λ with the magnitude of deflection in $V_m$, to ensure comparable influence of SCRE for each cell model, the $[Ca^{2+}]_{SR}$ was set to exactly 1.05 mM 1 ms prior to the implemented SRF. The latency ($t_i$) was kept constant, as synchronisation is only a relevant factor in tissue simulations. In tissue models, the median of the duration distribution was varied (controlling λ) and the width of the $t_i$ distribution was also varied to control synchronisation degree. More details are provided in Supporting information, Text S1.

A strategy was implemented to facilitate efficiency and feasibility of this large-scale study: single-cell models were paced for 200 beats under each condition required, and the state variables saved to file. These were the read-in to start new simulations from this pre-paced state. In single cell simulations, 100 runs were performed at each $[Ca^{2+}]_{SR}$ to calculate $P_{TA}$. In tissue simulations, the single-cell state files were originally read in, and five beats were applied to the tissue model before saving the entire tissue state. This was then read in to start new tissue simulations from a pre-paced steady state. An initial pass of one simulation was performed at each $[Ca^{2+}]_{SR}$ to identify the threshold region. 30 simulations were then performed in total at each $[Ca^{2+}]_{SR}$ around this threshold region in order to calculate $P_{TA}$. In results simulations, a single paced beat was applied after reading in the state files, and the model was then left quiescent for a total simulation time of 2000 ms to analyse the impact of SCRE occurring within this time.

## Results

### SCRE manifests differently in different regional cell models

In all cell models, $P_{TA}$ increased with higher $[Ca^{2+}]_{SR}$ load (Fig. 3*Aa*). Only small differences were observed between the RA, LA, and CT-BB cell models, whereas PV cells exhibited a lower $[Ca^{2+}]_{SR}$ threshold for TA (defined as the $[Ca^{2+}]_{SR}$ at which $P_{TA} = 0.5$; threshold = 1.186 mM in the RA compared to 1.164 mM in the PVs). This is reflected in the correlation of the magnitude of voltage deflection against λ (Fig. 3*Ab*), wherein PV cells exhibited larger deflections and exceeded the threshold for TA at longer durations than the surrounding atria. Cell models of the RA, LA, and CT-BB all exhibited a stepwise transition from DADs ($V_{m,max} < \sim -60$ mV) to TA ($V_{m,max} > \sim -20$ mV). Conversely, the PVs exhibited a smooth transition from DADs to TA, wherein large, sub-threshold DADs (those with a peak substantially above −60 mV) were observed within a small window of λ (Fig. 3*Ab*, *c*).

Further investigation revealed that the RMP and reduced $I_{K1}$ contributed to both of these features (Fig. 3*B*). Whereas both are related to $I_{K1}$ activity in this study, their impact can be considered separately (RMP could be affected by modifying many currents other than $I_{K1}$). First, the less negative RMP means that the diastolic voltage in PV cells is closer to the threshold for activation of $I_{Na}$ (∼−60 mV) than the rest of the atria. Thus, a smaller amplitude DAD was required to surpass this threshold. Second, the smaller outward current opposing this DAD as a consequence of reduced $I_{K1}$ means that the same size spontaneous $Ca^{2+}$ transient (and thus $I_{NaCa}$ activation) resulted in a steeper and larger amplitude DAD.

The relative contribution of reduced $I_{K1}$ and less hyperpolarised RMP were assessed by including these changes separately and together in the RA cell model, i.e. by imposing a voltage shift of $I_{K1}$ (in the range 0–10 mV) to change RMP (but preserve the magnitude of $I_{K1}$ in the RMP voltage range), and scaling of the magnitude of $I_{K1}$ (in the range 100% to 50%). Implementing either factor individually reproduced the key features observed in the PVs: left-ward shifted $[Ca^{2+}]_{SR}$ dependence and right-ward shifted λ dependence. Implementation of either individually led to shifts that were over halfway between the control case and the case where both were implemented together, indicating that the combined effect is incrementally smaller than the initial effect of either modification. Both effects show similar continuous dependence on the parameter changes (Fig. 3*C*).

### Cellular differences are enhanced in tissue

In idealised 2D tissue, the dependence of $P_{TA}$ on $[Ca^{2+}]_{SR}$ was substantially steeper for all cell types compared to single cells (Fig. 4*Aa*). The differences between the PV and other regions were enhanced: the difference in $[Ca^{2+}]_{SR}$ threshold for SCRE was approximately double in 2D tissue that of single cells (0.040 mM *vs.* 0.022 mM). This is a consequence of the higher $P_{TA}$ at lower $[Ca^{2+}]_{SR}$ in the PV region, combined with a less constrained requirement

for the number of cells undergoing TA in PV tissue: the threshold for tissue focal excitation in the PV model occurred at a $[Ca^{2+}]_{SR}$ value that corresponded to a lower cellular $P_{TA}$ compared to the equivalent in the RA model. In the PVs, the threshold for tissue excitation occurred at 1.165 mM, which corresponded to a cellular $P_{TA}$ of ∼0.5; in the RA it occurred at 1.205 mM, which corresponded to a cellular $P_{TA}$ of ∼0.75 (Fig. 4*Aa*, illustrated by the dotted lines). In other words, in the PV tissue model, only ∼50% of the nodes were required to undergo SCRE of sufficient magnitude to induce cellular TA in order for this to manifest in tissue, whereas in the RA, ∼75% of the nodes were required to do so. The change in magnitude of $I_{K1}$ has more impact than the RMP shift, compared to in a single cell where they had similar impacts (Fig. 4*Ab*). The increased propensity for PVs to undergo focal excitations was independent of the level of synchronisation, although large subthreshold DADs become more prominent as synchronisation was reduced (Fig. 4*B*).

## Cellular factors combine to preferentially locate focal excitations to the PV sleeves

The dependence of $P_{TA}$ on $[Ca^{2+}]_{SR}$ was steep in the 3D atrial model, comparable to the 2D tissue models (Fig. 5*Aa*). In the 3D homogeneous atria (wherein all

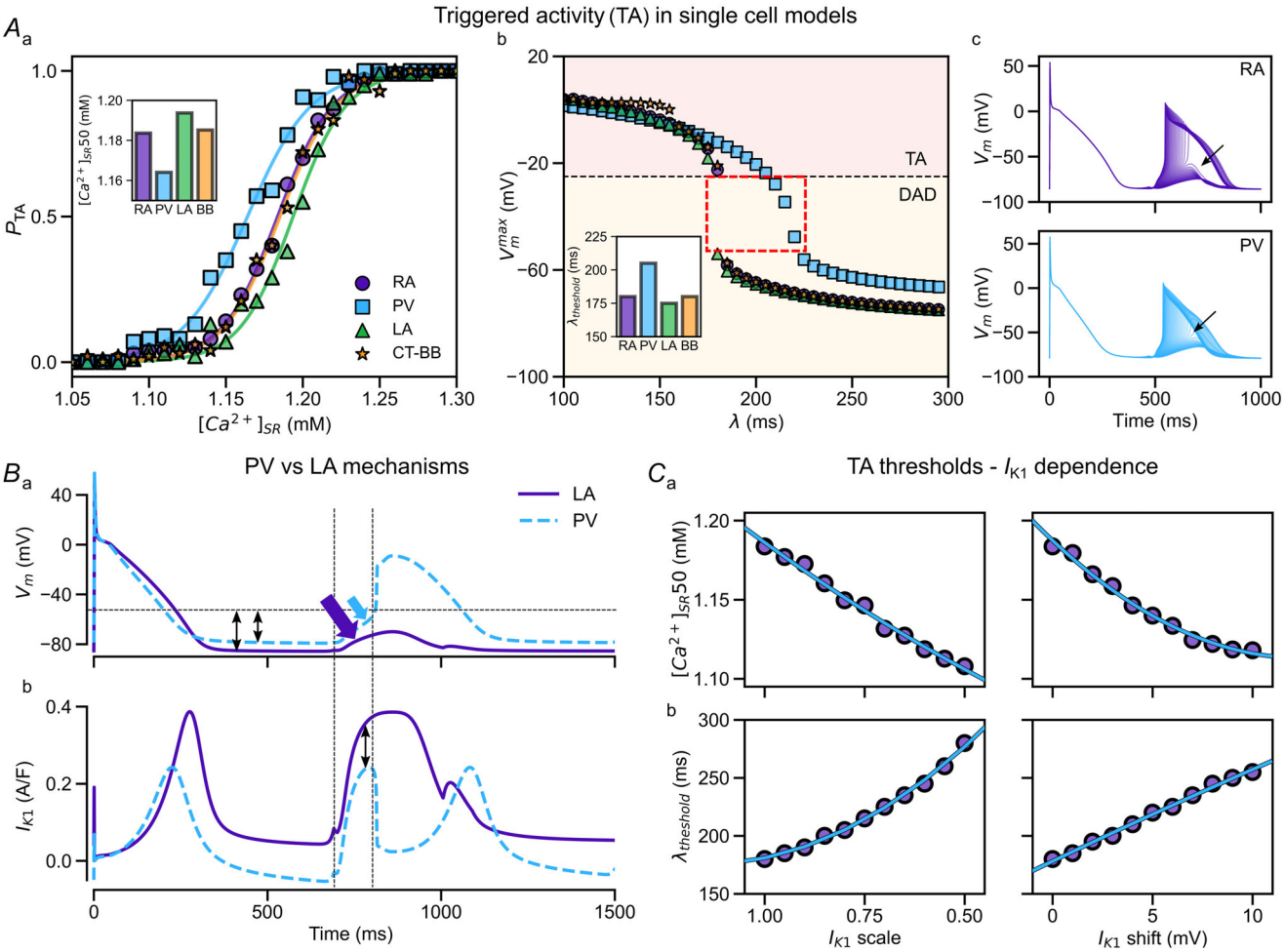


**Figure 3. Single-cell triggered activity**
*Aa*, the probability of triggered action potentials, $P_{TA}$, as a function of $[Ca^{2+}]_{SR}$ for the four cell types. Inset shows the $[Ca^{2+}]_{SR}50$ (the $[Ca^{2+}]_{SR}$ concentration at which $P_{TA}$ is 0.5) for each. *b*, the peak voltage as a function of λ (waveform duration); inset shows the threshold for TA (defined as $V_{m,max} > -25$ mV). The dashed red box indicates large non-TA-inducing DADs occurring in the PV but not in other regions. *c*, overlays of APs induced across the range of λ values for the RA and PV, illustrating the stepwise transition to TA in the RA *vs*. the continuous transition in the PVs. *B*, illustration of the combined impact of reduced $I_{K1}$ and less hyperpolarised RMP on the development of TA, through comparison of the PV dynamics *vs*. the LA. Double arrows show the proximity of the RMP to the threshold for $I_{Na}$ activation, and block arrows indicate the impact of the different magnitudes of $I_{K1}$ operating against the DAD in each condition. *C*, $[Ca^{2+}]_{SR}50$ (1) and λ threshold (2) dependence on $I_{K1}$ scaling factor (100% to 50%) and voltage shift (0–10 mV). [Colour figure can be viewed at wileyonlinelibrary.com]

nodes are described by the RA cell model), all focal excitations originated proximate to the SAN (Fig. 5*Ab* and *B*). This is a direct consequence of the SAN being the initial stimulus site. These regions undergo SCRE earlier, since SCRE timing is relative to the previous excitation time. Therefore, when SCRE is sufficient to induce a focal excitation, it occurs preferentially from these sites. Preliminary tests in which the pacing was applied to a different region support this explanation: focal excitations preferentially emerged from close to the previous stimulation site.

The inclusion of inter-cellular heterogeneity in 3D atrial models resulted in a large leftward shift of the $[Ca^{2+}]_{SR}$ dependence of focal excitations, almost double the difference observed in 2D tissue (Fig. 5*Aa*). Focal excitations were now preferentially localised in the PVs (Fig. 5*Ab*). In these simulations, all focal excitations originated either from the PVs (at lower $[Ca^{2+}]_{SR}$, where cellular heterogeneity is most important) or proximate to the SAN (at higher $[Ca^{2+}]_{SR}$, where the timing considerations described above become important). Excitations could originate from either PV, and were also occasionally observed at both simultaneously (Fig. 5*B*).

Further focal locations were observed in homogeneous simulations that varied the synchronisation and λ distributions at a fixed $[Ca^{2+}]_{SR}$ (Fig. 5*Ab* and *B*). Under these conditions, RAA focal locations were more common than in the $[Ca^{2+}]_{SR}$-dependent simulations, and additional sites at the LAA and PVs also emerged. Under heterogenous conditions, focal excitations emerged only from the PVs or SAN regions, as in the $[Ca^{2+}]_{SR}$-dependent conditions.

Inclusion or exclusion of anisotropy had a small impact on determining the specific locations of focal sources but did not affect the pattern observed or change the preference towards the PVs (not shown).

## Emergence of unidirectional conduction patterns

In a small subset of simulations, large, subthreshold DADs were observed in the PVs. These could propagate into the LA, inducing a focal excitation (Fig. 6*Aa*, *b*; Supporting

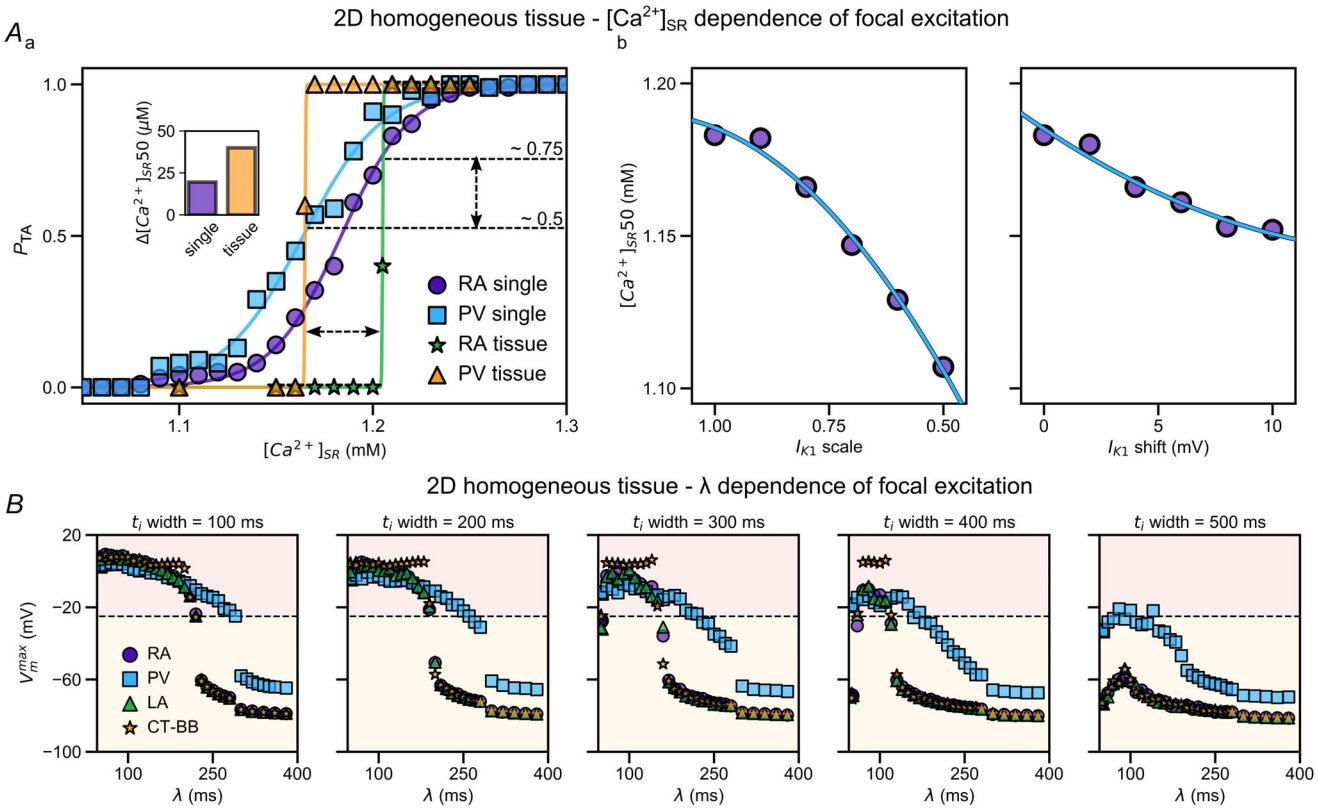


**Figure 4. Spontaneous arrhythmia triggers in 2D idealised tissue models**
*Aa*, dependence of the probability of focal excitation on $[Ca^{2+}]_{SR}$ for homogeneous tissue models comprising the RA or PVs. Single-cell and tissue dependence are both shown for clarity and comparison. Inset shows the $\Delta[Ca^{2+}]_{SR}50$ between RA and PV in single-cell and tissue. The dotted horizontal lines indicate the cellular $P_{TA}$ at the $[Ca^{2+}]_{SR}$ corresponding to the observed tissue $[Ca^{2+}]_{SR}50$ for each region. *b*, $[Ca^{2+}]_{SR}50$ for $I_{K1}$ scale and shift. *B*, dependence of voltage deflection magnitude on λ at different synchronisation amounts (timing distribution widths). [Colour figure can be viewed at wileyonlinelibrary.com]

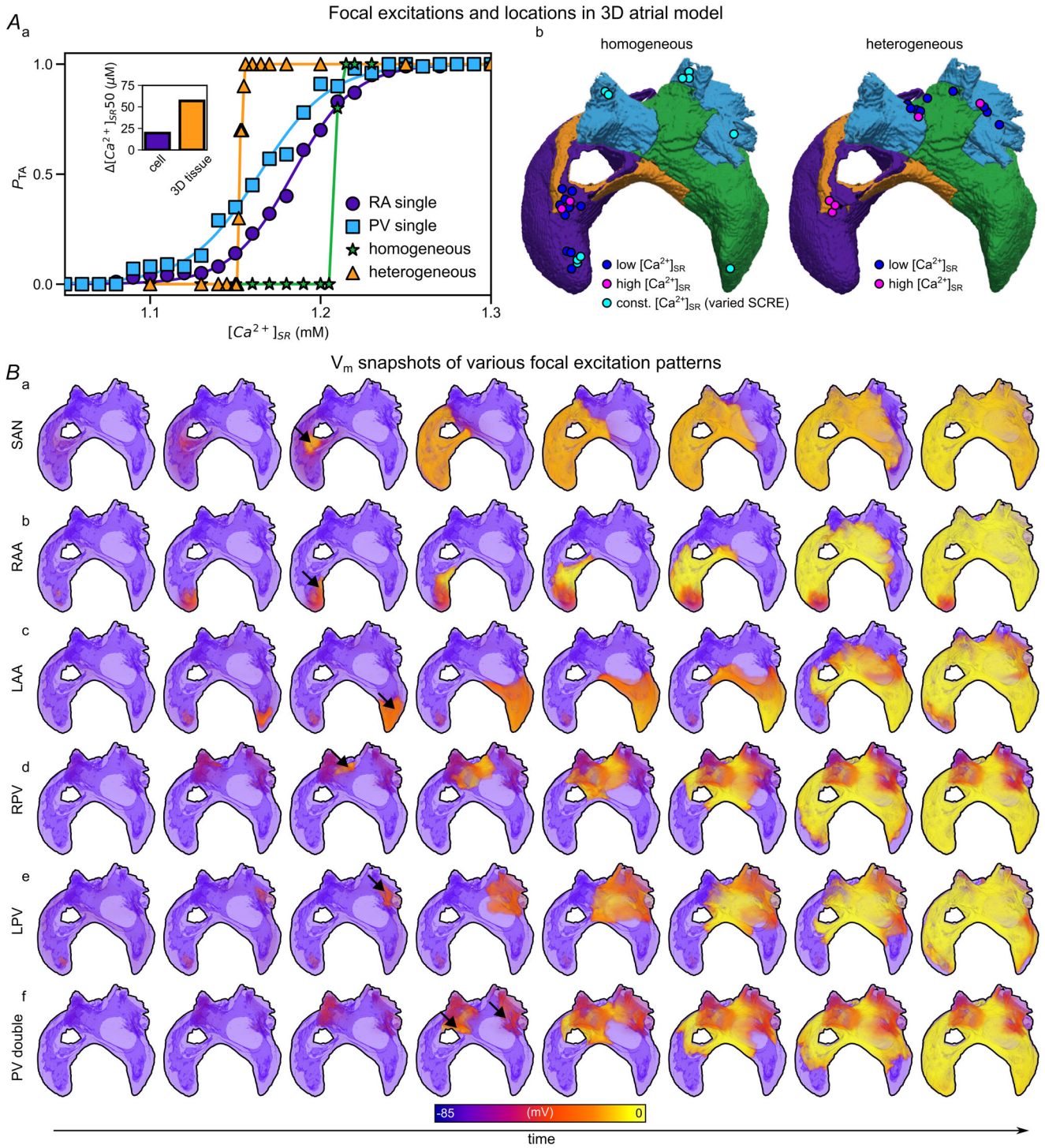


**Figure 5. Spontaneous arrhythmia triggers in full 3D canine atria**
*Aa*, $[Ca^{2+}]_{SR}$ dependence in homogeneous atria (all cells described by the RA cell model) and heterogeneous atria, with RA and PV single-cell TA shown for reference. *b*, locations of focal source in homogeneous and heterogeneous tissue, at low (dark blue circles) and high (pink circles) $[Ca^{2+}]_{SR}$ concentration, and with the $[Ca^{2+}]_{SR}$ held constant while SCRE dynamics were varied (light blue circles). *B*, voltage snapshots illustrating focal excitations emerging from the various locations observed in this study. Each focal excitation occurred over a different temporal range and the figure illustrates the qualitative excitation patterns that emerge; the specific snapshot timings have therefore been omitted for the purpose of clarity in the figure. [Colour figure can be viewed at wileyonlinelibrary.com]

information, Video S1). Through this mechanism, focal excitations could emerge unidirectionally: inactivation of $I_{Na}$ due to these large DADs (observed exclusively in the PV region, Fig. 3*Ac*) prevented a full excitation emerging in this region; however, the voltage deflections could be of sufficient magnitude that they could induce a full focal excitation at the border of the PVs and LA that then propagated throughout the LA, while being initially prevented from entering the PVs. This mechanism was further demonstrated in an idealised scenario (Fig. 6*B*): in homogeneous 2D tissue comprising only PV cell models, SCRE was assigned only to an inner region of the tissue, such that the outer region does not undergo SCRE and therefore no inactivation of $I_{Na}$ occurs. In these simulations, large DADs were observed in the SCRE region but did not induce a focal excitation in this

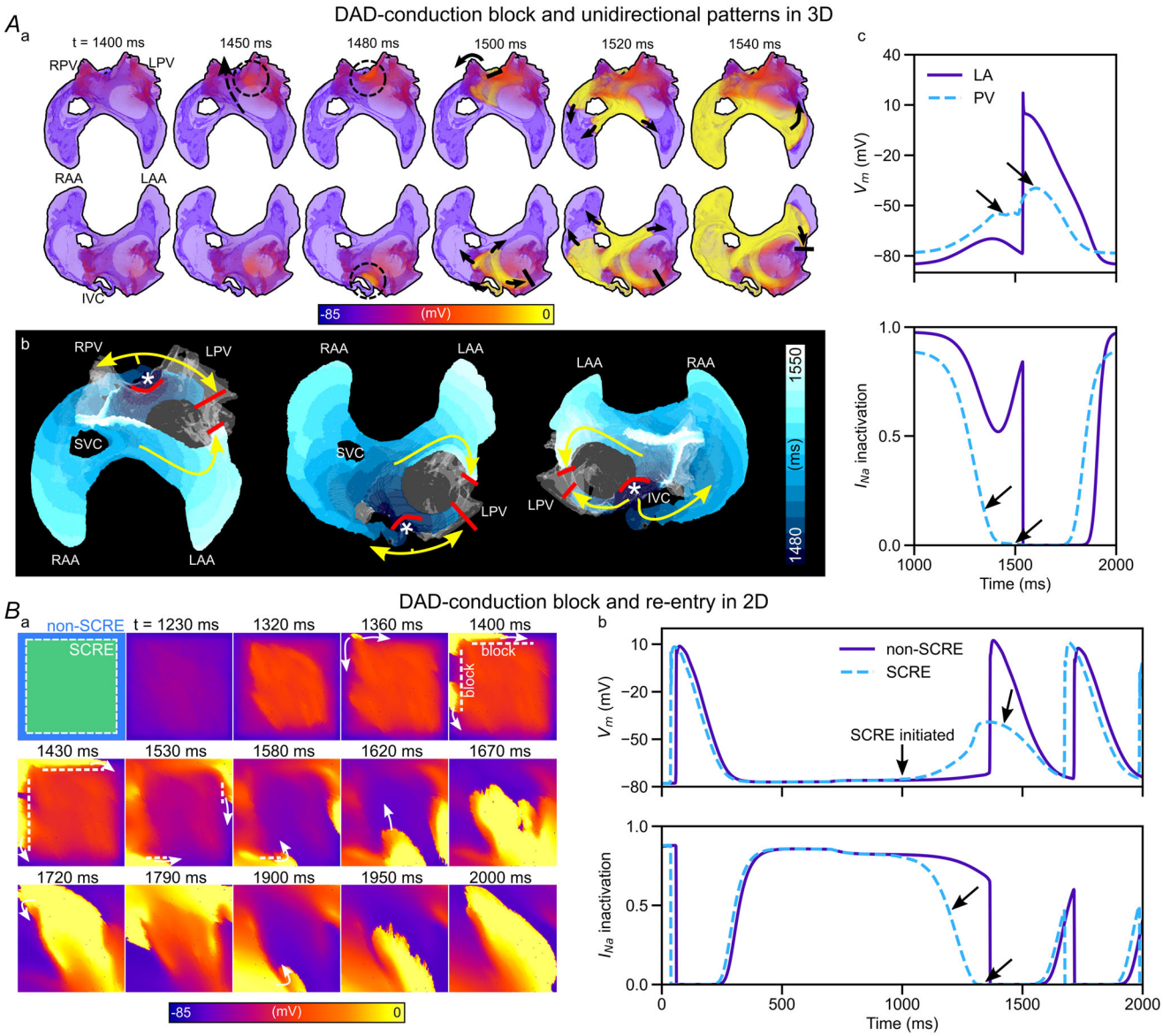


**Figure 6. Unidirectional excitation patterns**
*Aa*, voltage snapshots of a unidirectional conduction pattern that emerges from subthreshold DADs in the PVs travelling into the LA in the 3D canine atrial model. *b*, corresponding activation pattern from multiple views. *c*, AP traces (upper) and $I_{Na}$ inactivation state (lower) from a node in the LA and PV region, illustrating non-excitation DADs in the PV. $I_{Na}$ inactivation state is the combination of the inactivation gates, corresponding to $h \times j$ in traditional terminology ($I_{Na\_vi\_1} \times I_{Na\_vi\_2}$ using the terminology conventions implemented in the associated source code). *B*, demonstration of the same mechanism occurring in idealised 2D tissue in which SCRE were not induced in the boundary regions. This simulation shown also included fibrosis as the slowed conduction promoted the re-entrant pattern which best illustrates the potential consequences of this mechanism. [Colour figure can be viewed at wileyonlinelibrary.com]

region. When these DADs reached the non-SCRE region, they emerged as a focal excitation which propagated asymmetrically in a re-entrant-like circuit.

## Impact of fibrosis on focal and re-entrant excitations

The inclusion of fibrosis had a marked impact on the vulnerability to focal excitations as well as the dynamics that result from such excitations. In 2D in the RA model, the inclusion of fibrosis left-shifted the dependence of focal excitations on $[Ca^{2+}]_{SR}$ (Fig. 7*Aa*). It also resulted in the emergence of lower probability events at low $[Ca^{2+}]_{SR}$ loads (Fig. 7*Ab*), compared to the stepwise dependence observed in control tissue. At higher $[Ca^{2+}]_{SR}$ loads, trigger–substrate interactions, wherein DADs in one region could block focal excitations emerging from another region, led to complex, re-entrant-like excitation patterns (Fig. 7*Ac–d*; Supporting information, Video S2).

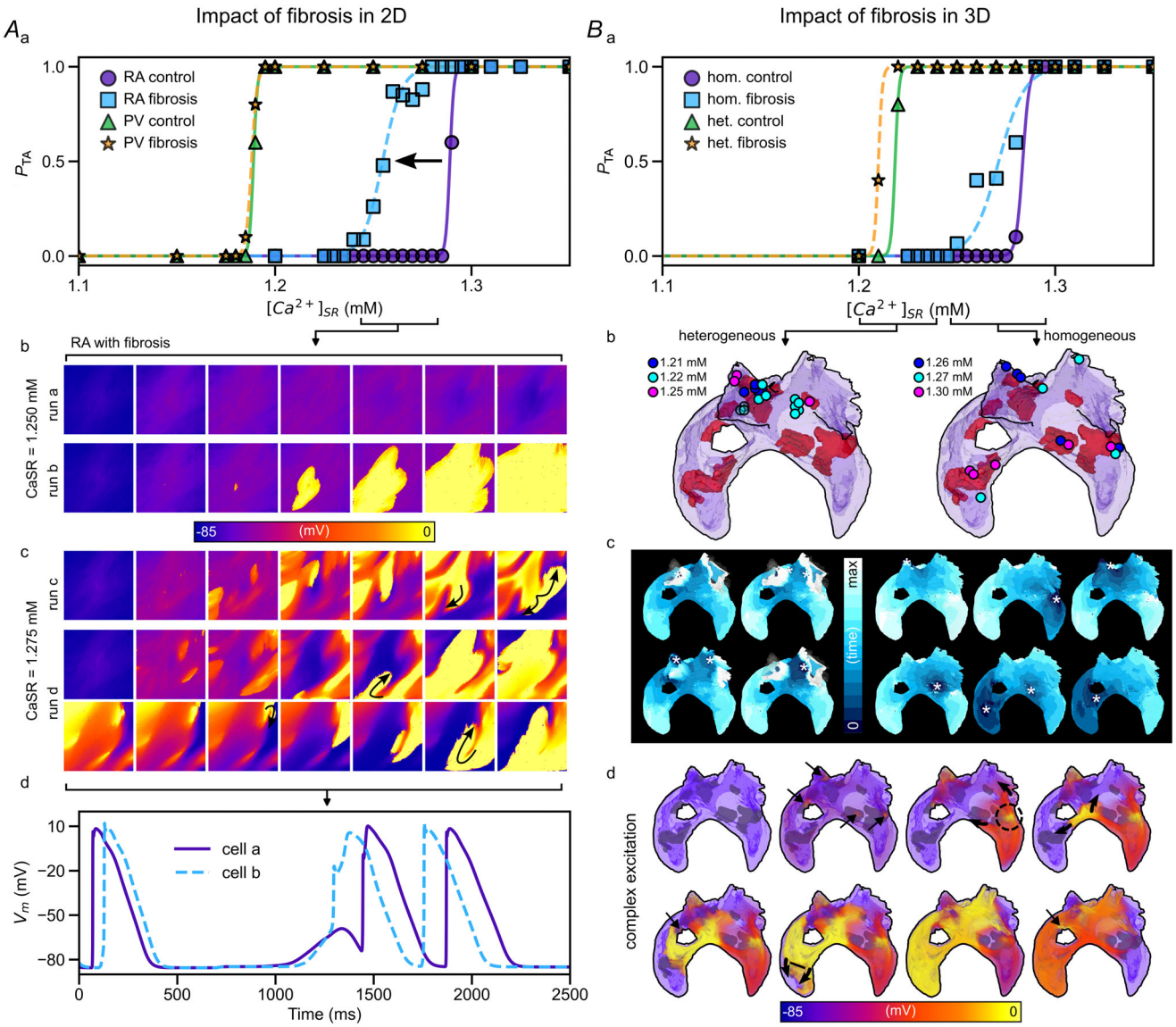


**Figure 7. Impact of fibrosis on atrial excitation patterns**
*Aa*, impact of fibrosis in homogeneous 2D sheets on the $[Ca^{2+}]_{SR}$ dependence of focal excitation. *b*, voltage snapshots observed in two different simulations in the $[Ca^{2+}]_{SR}$ region in which TA exhibited probabilistic dynamics, showing a failed excitation (upper) and full focal excitation (lower). *d*, illustration of more complex excitation patterns emerging in the presence of fibrosis at higher $[Ca^{2+}]_{SR}$, illustrating two independent simulations. *Ba*, impact of fibrosis in the 3D atrial model on the $[Ca^{2+}]_{SR}$ dependence of focal excitation. *b*, locations of focal excitations in heterogeneous and homogenous 3D atrial models within the $[Ca^{2+}]_{SR}$ ranges illustrated. *c*, activation patterns associated with different focal locations. *d*, example of a complex, multi-foci activation sequence occurring in the presence of fibrosis. [Colour figure can be viewed at wileyonlinelibrary.com]

These results were reflected in the 3D atrial model. In the homogeneous scenario, the presence of fibrosis resulted in lower probability events that left-shifted the $[Ca^{2+}]_{SR}$ dependence (Fig. 7*Ba*). At these lower $[Ca^{2+}]_{SR}$ loads, focal excitations emerged preferentially from the various fibrosis patches throughout the atria; at higher $[Ca^{2+}]_{SR}$ loads, excitations emerged preferentially from fibrosis patches near the initial stimulus site at the SAN (Fig. 7*Bb*, *c*). In heterogeneous tissue, fibrosis had a smaller impact on the $[Ca^{2+}]_{SR}$ dependence but did preferentially locate the focal excitations to fibrosis patches within the PVs (Fig. 7*Ba*, *c*).

Complex re-entrant patterns were not observed in our simulations in the 3D atrial model to the same degree as in the 2D model (i.e. there were no clear re-entrant circuits). However, complex, multi-focal patterns with some degree of wavebreak were observed (Fig. 7*Bd*; Supporting information, Video S3).

## Discussion

### Summary of main findings

The main findings of our analysis are: (1) the lower expression of $I_{K1}$ and less hyperpolarised RMP in the PV preferentially locates focal excitations to the PV region in electrically heterogeneous 3D atria (Figs 3–5); (2) inactivation of $I_{Na}$ as a consequence of the less hyperpolarised RMP promoted large, subthreshold DADs in the PV region that could lead to complex, unidirectional excitation patterns that did not depend on refractoriness (Fig. 6); (3) anatomical features played a much less important role than electrophysiology in controlling focal excitation location in the structurally healthy 3D atria (Fig. 5); and (4) fibrosis in structurally remodelled atria promoted localised focal excitations and wavebreaks, generating AF-like excitation patterns (Fig. 7).

### RMP and $I_{K1}$ in the PVs can explain the localisation of AF triggers in this region

AF sources are commonly associated with the PV sleeves (Haïssaguerre et al., 1998; Sanders et al., 2005). In previous studies, we and others have demonstrated that local APD gradients and the shorter APD of the PVs compared to the surrounding atria could promote sustained re-entrant excitation anchored to the PVs (Aslanidi, Colman, et al., 2013; Cherry et al., 2007; Colman et al., 2013; Roney et al., 2018; Varela et al., 2016). The present study demonstrates that electrophysiological features of the PVs also promote the emergence of focal excitations from this region, which can trigger the subsequent re-entrant excitations. This was a result of RMP differences and $I_{K1}$ heterogeneity between the PVs and atria. No other features were required to locate focal excitations to the PVs, demonstrating that these RMP differences in combination with cellular SCRE are sufficient conditions to promote AF triggers in the PVs. Other features, such as local innervation (Chen et al., 2014; Linz et al., 2014) or stretch (Egorov et al., 2019; Gottlieb et al., 2023; Varela et al., 2021), may or may not be more important for the induction of AF, but they are not *required* to reproduce our observations.

It is important to bear in mind that RMP and $I_{K1}$ are closely related, and that in the present study, either the magnitude or reversal potential of $I_{K1}$ was used to control the RMP. However, these are considered separately as they result in two different, important features: distance between RMP and activation threshold for $I_{Na}$, and the magnitude of current opposing the DAD, respectively. In the atria, and in particularly in the context of the PVs, $I_{K1}$ indeed dominates both features (Ehrlich et al., 2003). However, in other regions of the heart or disease conditions, both features could be impacted by currents other than $I_{K1}$, and the mechanisms can be generalised to other factors that may be more important in modulating RMP. The mechanisms we have revealed, we argue, are a consequence of RMP and magnitude of current that opposes a DAD, and not specifically only applicable in the context of $I_{K1}$ function.

### Inactivation of $I_{Na}$ due to higher RMP enables large but subthreshold DADs

Recent studies have shown that DADs which inactivate $I_{Na}$ can simultaneously cause both focal excitations and conduction block, highlighting the importance of this novel mechanism (Campos et al., 2017, 2018, 2022; Liu et al., 2015). Our study adds further weight to the impact of subthreshold DADs, while also revealing a novel mechanism of non-refractory induced unidirectional conduction block: the propagation of subthreshold DADs in one region that emerge as full excitations into another adjacent region. These DADs occur near the threshold for SCRE, which is a less constrained condition than that required for suprathreshold DADs. The latter would be required for a rapidly timed focal excitation that interacts with cellular refractoriness within a small vulnerability window to induce unidirectional conduction. This subthreshold DAD mechanism may therefore loosen the constraints on the conditions that are required to induce arrhythmia. This feature is also unique to the PVs in the structurally normal atria (i.e. no structural remodelling or fibrosis), providing yet another mechanism that can contribute to the preferential localisation of AF triggers in the PV region, especially in paroxysmal AF (Haïssaguerre et al., 1998).

## Fibrosis promotes focal excitations and trigger-substrate interactions

Fibrosis has long been associated with structural remodelling of the atria (Akoum et al., 2011), as well as changes of the gap junction distribution in atrial tissue during AF (Kostin et al., 2002), and therefore changes in atrial conduction patterns (McDowell et al., 2013). The loss of inter-cellular connectivity associated with fibrosis, in particular in the transverse direction (de Jong et al., 2011), also promoted the emergence of focal excitations in our 2D and 3D atrial models. Specifically, preferential loss of transverse connections created a condition wherein the tissue structure was characterised by multiple, loosely connected 1D strands (Xie et al., 2010). The lesser electrotonic suppression observed in 1D strands compared to 3D fully connected tissue enabled SCRE of a given size to result in larger-amplitude DADs. The latter more easily reached the threshold for focal excitations, resulting in a leftward shift of the $[Ca^{2+}]_{SR}$ dependence in homogeneous tissue. This effect was markedly largest in atrial tissue compared to the PVs, where significantly less hyperpolarised RMP overrides the impact of this reduced electrotonic coupling.

It is notable that the impact of fibrosis in the entire 3D atria was smaller than that observed in 2D atrial tissues. This observation could be explained by the relative different proportions of fibrotic tissue in the 2D *vs*. 3D models: in 2D, the whole of the tissue was treated as being in a fibrotic state (see Methods), whereas in the 3D atrial model, the assigned patches of fibrosis based on EAM data made up a relatively small proportion of tissue (Fig. 1*Cd*).

The emergence of larger-amplitude DADs in fibrotic atrial regions outside of the PVs could inactivate $I_{Na}$ and block incoming focal excitations from other regions, through the same mechanism as described in the previous sections for the PVs. These conduction blocks can lead to the emergence of complex and re-entrant-like excitation patterns (Fig. 7). In both homogenous and heterogeneous tissues, focal excitations and the resultant re-entrant-like patterns were preferentially located in the regions of patchy fibrosis.

## Limitations

This study was aimed at assessing the interaction of cellular triggers with the tissue electrophysiological–anatomical substrate in AF, with the SCRE trigger events implemented using our recently proposed multi-scale method (Colman, 2019; Colman et al., 2021). This involved applying the statistics and dynamics of SCRE homogeneously throughout the atria, and therefore cellular electrophysiology differences that may promote SCRE in specific regions were not accounted for. Our results could potentially be enhanced by considering such cellular heterogeneity. For example, if the PVs were more prone to SCRE than the surrounding atria, as has been suggested by recent studies (Bond et al., 2020; Namekata et al., 2009; Rietdorf et al., 2014), then we would expect to see larger differences in the vulnerability to focal excitations between these regions than observed in this study. There are multiple factors, especially in the remodelled atria, which could lead to a local increase in SCRE, such $Ca^{2+}$ handling remodelling (Molina et al., 2018), that need to be investigated in more detail at the cellular level before they can be implemented in tissue models.

Our study did not include progressive AF remodelling effects on ionic channels (Grandi et al., 2011; Varela et al., 2016; Workman et al., 2001), which may have important implications due to its reported impact on $I_{K1}$ and hyperpolarisation of the RMP (Nattel et al., 2008). Inclusion of such remodelling adds complexity but would enable a more complete analysis of the genesis of AF, including the conditions that promote both focal excitations and sustained re-entrant activity.

Atrial anatomical microstructure can also play an important role in sustaining re-entrant drivers for AF (Hansen et al., 2015). The necessary downsampling of the original imaging data into the simulation geometry (to the uniform resolution of $\Delta x = 0.3$ mm) in this study may obscure higher resolution features in our simulations that could be important, for example micro-re-entrant drivers or local synchronisation of triggers. Future studies could focus on smaller areas of tissue using higher resolution reconstructions (available in the original imaging data of Aslanidi, Nikolaidou, et al., 2013) to study these features in more detail. Moreover, structural remodelling was only implemented based on patchy fibrosis from a single sample. Future studies could include remodelling of atrial anatomy, anisotropy and fibroblast–myocyte coupling, which have been shown to be important for re-entrant dynamics (McDowell et al., 2013; Morgan et al., 2016).

## Conclusions

Simulations of 3D canine atria revealed that electrophysiological features of PV myocytes, such as the RMP, preferentially locate focal excitations to this region and promote the emergence of complex, re-entrant-like excitation patterns that do not depend on refractory properties. Fibrosis further promotes these focal triggers, in addition to the known effect of sustaining re-entrant drivers for AF.

## References


Akoum, N., Daccarett, M., McGann, C., Segerson, N., Vergara, G., Kuppahally, S., Badger, T., Burgon, N., Haslam, T., Kholmovski, E., Macleod, R., & Marrouche, N. (2011). Atrial fibrosis helps select the appropriate patient and strategy in catheter ablation of atrial fibrillation: A DE-MRI guided approach. *Journal of Cardiovascular Electrophysiology*, **22**(1), 16–22.

Anyukhovsky, E. P., Sosunov, E. A., Plotnikov, A., Gainullin, R. Z., Jhang, J. S., Marboe, C. C., & Rosen, M. R. (2002). Cellular electrophysiologic properties of old canine atria provide a substrate for arrhythmogenesis. *Cardiovascular Research*, **54**(2), 462–469.

Aslanidi, O. V., Al-Owais, M., Benson, A. P., Colman, M., Garratt, C. J., Gilbert, S. H., Greenwood, J. P., Holden, A. V., Kharche, S., Kinnell, E., Pervolaraki, E., Plein, S., Stott, J., & Zhang, H. (2012). Virtual tissue engineering of the human atrium: Modelling pharmacological actions on atrial arrhythmogenesis. *European Journal of Pharmaceutical Sciences*, **46**(4), 209–221.

Aslanidi, O. V., Colman, M. A., Stott, J., Dobrzynski, H., Boyett, M. R., Holden, A. V., & Zhang, H. (2011). 3D virtual human atria: A computational platform for studying clinical atrial fibrillation. *Progress in Biophysics and Molecular Biology*, **107**(1), 156–168.

Aslanidi, O. V., Colman, M. A., Varela, M., Zhao, J., Smaill, B. H., Hancox, J. C., Boyett, M. R., & Zhang, H. (2013). Heterogeneous and anisotropic integrative model of pulmonary veins: Computational study of arrhythmogenic substrate for atrial fibrillation. *Interface Focus*, **3**(2), 20120069.

Aslanidi, O. V., Nikolaidou, T., Zhao, J., Smaill, B. H., Gilbert, S. H., Holden, A. V., Lowe, T., Withers, P. J., Stephenson, R. S., Jarvis, J. C., Hancox, J. C., Boyett, M. R., & Zhang, H. (2013). Application of micro-computed tomography with iodine staining to cardiac imaging, segmentation, and computational model development. *IEEE Transactions on Medical Imaging*, **32**(1), 8–17.

Bond, R. C., Choisy, S. C., Bryant, S. M., Hancox, J. C., & James, A. F. (2020). Ion currents, action potentials, and noradrenergic responses in rat pulmonary vein and left atrial cardiomyocytes. *Physiological Reports*, **8**(9), e14432.

Burashnikov, A., Mannava, S., & Antzelevitch, C. (2004). Transmembrane action potential heterogeneity in the canine isolated arterially perfused right atrium: Effect of IKr and IKur/Ito block. *American Journal of Physiology-Heart and Circulatory Physiology*, **286**(6), H2393–H2400.

Burdett, P., & Lip, G. Y. H. (2022). Atrial fibrillation in the UK: Predicting costs of an emerging epidemic recognizing and forecasting the cost drivers of atrial fibrillation-related costs. *European Heart Journal-Quality of Care & Clinical Outcomes*, **8**(2), 187–194.

Camm, A. J., Kirchhof, P., Lip, G. Y., Schotten, U., Savelieva, I., Ernst, S., Van Gelder, I. C., Al-Attar, N., Hindricks, G., Prendergast, B., Heidbuchel, H., Alfieri, O., Angelini, A., Atar, D., Colonna, P., De Caterina, R., De Sutter, J., Goette, A., Gorenek, B., … Rutten, F. H. (2010). Guidelines for the management of atrial fibrillation: The task force for the management of atrial fibrillation of the European Society of Cardiology (ESC). *European Heart Journal*, **31**(19), 2369–2429.

Campos, F. O., Shiferaw, Y., Prassl, A. J., Boyle, P. M., Vigmond, E. J., & Plank, G. (2015). Stochastic spontaneous calcium release events trigger premature ventricular complexes by overcoming electrotonic load. *Cardiovascular Research*, **107**(1), 175–183.

Campos, F. O., Shiferaw, Y., Vigmond, E. J., & Plank, G. (2017). Stochastic spontaneous calcium release events and sodium channelopathies promote ventricular arrhythmias. *Chaos: An Interdisciplinary Journal of Nonlinear Science*, **27**(9), 093910.

Campos, F. O., Shiferaw, Y., Weber dos Santos, R., Plank, G., & Bishop, M. J. (2018). Microscopic isthmuses and fibrosis within the border zone of infarcted hearts promote calcium-mediated ectopy and conduction block. *Frontiers in Physics*, **6**, 00057.

Campos, F. O., Shiferaw, Y., Whitaker, J., Plank, G., & Bishop, M. J. (2022). Subthreshold delayed afterdepolarizations provide an important arrhythmogenic substrate in the border zone of infarcted hearts. *Heart Rhythm*, **20**(2), 299–306.

Chen, P.-S., Chen, L. S., Fishbein, M. C., Lin, S.-F., & Nattel, S. (2014). Role of the autonomic nervous system in atrial fibrillation. *Circulation Research*, **114**(9), 1500–1515.

Cherry, E. M., Ehrlich, J. R., Nattel, S., & Fenton, F. H. (2007). Pulmonary vein reentry—Properties and size matter: Insights from a computational analysis. *Heart Rhythm*, **4**(12), 1553–1562.

Colman, M. A. (2019). Arrhythmia mechanisms and spontaneous calcium release: Bi-directional coupling between re-entrant and focal excitation. *PLoS Computational Biology*, **15**(8), e1007260.

Colman, M. A., Alvarez-Lacalle, E., Echebarria, B., Sato, D., Sutanto, H., & Heijman, J. (2022). Multi-scale computational modeling of spatial calcium handling from nanodomain to whole-heart: Overview and perspectives. *Frontiers in Physiology*, **13**, 836622.

Colman, M. A., Aslanidi, O. V., Kharche, S., Boyett, M. R., Garratt, C., Hancox, J. C., & Zhang, H. (2013). Pro-arrhythmogenic effects of atrial fibrillation-induced electrical remodelling: Insights from the three-dimensional virtual human atria. *The Journal of Physiology*, **591**(17), 4249–4272.

Colman, M. A., & Benson, A. P. (2023). A simple approach for image-based modelling of the heart that enables robust simulation of highly heterogeneous electrical excitation. *Scientific Reports*, **13**(1), 15119.

Colman, M. A., Holmes, M., Whittaker, D. G., Jayasinghe, I., & Benson, A. P. (2021). Multi-scale approaches for the simulation of cardiac electrophysiology: I – Sub-cellular and stochastic calcium dynamics from cell to organ. *Methods (San Diego, Calif.)*, **185**, 49–59.

Colman, M. A., Varela, M., Hancox, J. C., Zhang, H., & Aslanidi, O. V. (2014). Evolution and pharmacological modulation of the arrhythmogenic wave dynamics in canine pulmonary vein model. *Europace*, **16**(3), 416–423.

de Bakker, J. M. T., Ho, S. Y., & Hocini, M. (2002). Basic and clinical electrophysiology of pulmonary vein ectopy. *Cardiovascular Research*, **54**(2), 287–294.

de Jong, S., van Veen, T. A. B., van Rijen, H. V. M., & de Bakker, J. M. T. (2011). Fibrosis and cardiac arrhythmias. *Journal of Cardiovascular Pharmacology*, **57**(6), 630–638.

Dössel, O., Krueger, M. W., Weber, F. M., Wilhelms, M., & Seemann, G. (2012). Computational modeling of the human atrial anatomy and electrophysiology. *Medical & Biological Engineering & Computing*, **50**(8), 773–799.

Dössel, O., Luongo, G., Nagel, C., & Loewe, A. (2021). Computer modeling of the heart for ECG interpretation—A review. *Hearts*, **2**(3), 350–368.

Egorov, Y. V., Lang, D., Tyan, L., Turner, D., Lim, E., Piro, Z. D., Hernandez, J. J., Lodin, R., Wang, R., Schmuck, E. G., Raval, A. N., Ralphe, C. J., Kamp, T. J., Rosenshtraukh, L. V., & Glukhov, A. V. (2019). Caveolae-mediated activation of mechanosensitive chloride channels in pulmonary veins triggers atrial arrhythmogenesis. *Journal of the American Heart Association*, **8**(20), e012748.

Ehrlich, J. R., Cha, T.-J., Zhang, L., Chartier, D., Melnyk, P., Hohnloser, S. H., & Nattel, S. (2003). Cellular electrophysiology of canine pulmonary vein cardiomyocytes: Action potential and ionic current properties. *The Journal of Physiology*, **551**(Pt 3), 801–813.

Eisner, D., Bode, E., Venetucci, L., & Trafford, A. (2013). Calcium flux balance in the heart. *Journal of Molecular and Cellular Cardiology*, **58**, 110–117.

Eisner, D. A., Kashimura, T., Venetucci, L. A., & Trafford, A. W. (2009). From the ryanodine receptor to cardiac arrhythmias. *Circulation Journal*, **73**(9), 1561–1567.

Feng, J., Yue, L., Wang, Z., & Nattel, S. (1998). Ionic mechanisms of regional action potential heterogeneity in the canine right atrium. *Circulation Research*, **83**(5), 541–551.

Gottlieb, L. A., Coronel, R., & Dekker, L. R. C. (2023). Reduction in atrial and pulmonary vein stretch as a therapeutic target for prevention of atrial fibrillation. *Heart Rhythm*, **20**(2), 291–298.

Grandi, E., Pandit, S. V., Voigt, N., Workman, A. J., Dobrev, D., Jalife, J., & Bers, D. M. (2011). Human atrial action potential and $Ca^{2+}$ model. *Circulation Research*, **109**(9), 1055–1066.

Greene, D., Kaboudian, A., Wasserstrom, J. A., Fenton, F. H., & Shiferaw, Y. (2022). Voltage-mediated mechanism for calcium wave synchronization and arrhythmogenesis in atrial tissue. *Biophysical Journal*, **121**(3), 383–395.

Guerra, J. M., Everett, T. H., Lee, K. W., Wilson, E., & Olgin, J. E. (2006). Effects of the gap junction modifier rotigaptide (ZP123) on atrial conduction and vulnerability to atrial fibrillation. *Circulation*, **114**(2), 110–118.

Haïssaguerre, M., Jaïs, P., Shah, D. C., Takahashi, A., Hocini, M., Quiniou, G., Garrigue, S., Le Mouroux, A., Le Métayer, P., & Clémenty, J. (1998). Spontaneous initiation of atrial fibrillation by ectopic beats originating in the pulmonary veins. *New England Journal of Medicine*, **339**(10), 659–666.

Hansen, B. J., Zhao, J., Csepe, T. A., Moore, B. T., Li, N., Jayne, L. A., Kalyanasundaram, A., Lim, P., Bratasz, A., Powell, K. A., Simonetti, O. P., Higgins, R. S. D., Kilic, A., Mohler, P. J., Janssen, P. M. L., Weiss, R., Hummel, J. D., & Fedorov, V. V. (2015). Atrial fibrillation driven by micro-anatomic intramural re-entry revealed by simultaneous sub-epicardial and sub-endocardial optical mapping in explanted human hearts. *European Heart Journal*, **36**(35), 2390–2401.

Heijman, J., Sutanto, H., Crijns, H., Nattel, S., & Trayanova, N. A. (2021). Computational models of atrial fibrillation: Achievements, challenges, and perspectives for improving clinical care. *Cardiovascular Research*, **117**(7), 1682–1699.

Heijman, J., Volders, P. G. A., Westra, R. L., & Rudy, Y. (2011). Local control of $\beta$-adrenergic stimulation: Effects on ventricular myocyte electrophysiology and Ca(2+)-transient. *Journal of Molecular and Cellular Cardiology*, **50**(5), 863–871.

Henry, A. D., MacQuaide, N., Burton, F. L., Rankin, A. C., Rowan, E. G., & Drummond, R. M. (2018). Spontaneous $Ca^{2+}$ transients in rat pulmonary vein cardiomyocytes are increased in frequency and become more synchronous following electrical stimulation. *Cell Calcium*, **76**, 36–47.

Jadidi, A. S., Lehrmann, H., Keyl, C., Sorrel, J., Markstein, V., Minners, J., Park, C. I., Denis, A., Jaïs, P., Hocini, M., Potocnik, C., Allgeier, J., Hochholzer, W., Herrera-Siklody, C., Kim, S., Omri, Y. E., Neumann, F. J., Weber, R., Haïssaguerre, M., & Arentz, T. (2016). Ablation of persistent atrial fibrillation targeting low-voltage areas with selective activation characteristics. *Circulation: Arrhythmia and Electrophysiology*, **9**(3), e002962.

Jæger, K. H., Edwards, A. G., Giles, W. R., & Tveito, A. (2022). Arrhythmogenic influence of mutations in a myocyte-based computational model of the pulmonary vein sleeve. *Scientific Reports*, **12**(1), 7040.

Kostin, S., Klein, G., Szalay, Z., Hein, S., Bauer, E. P., & Schaper, J. (2002). Structural correlate of atrial fibrillation in human patients. *Cardiovascular Research*, **54**(2), 361–379.

Landstrom, A. P., Dobrev, D., & Wehrens, X. H. T. (2017). Calcium signaling and cardiac arrhythmias. *Circulation Research*, **120**(12), 1969–1993.

Li, D., Fareh, S., Leung, T. K., & Nattel, S. (1999). Promotion of atrial fibrillation by heart failure in dogs: Atrial remodeling of a different sort. *Circulation*, **100**(1), 87–95.

Linz, D., Ukena, C., Mahfoud, F., Neuberger, H.-R., & Böhm, M. (2014). Atrial autonomic innervation: A target for interventional antiarrhythmic therapy? *Journal of the American College of Cardiology*, **63**(3), 215–224.

Liu, M. B., de Lange, E., Garfinkel, A., Weiss, J. N., & Qu, Z. (2015). Delayed afterdepolarizations generate both triggers and a vulnerable substrate promoting reentry in cardiac tissue. *Heart Rhythm*, **12**(10), 2115–2124.

Lopez-Perez, A., Sebastian, R., & Ferrero, J. M. (2015). Three-dimensional cardiac computational modelling: Methods, features and applications. *Biomedical Engineering Online [Electronic Resource]*, **14**, 35.

Mahida, S., Sacher, F., Derval, N., Berte, B., Yamashita, S., Hooks, D., Denis, A., Amraoui, S., Hocini, M., Haissaguerre, M., & Jais, P. (2015). Science linking pulmonary veins and atrial fibrillation. *Arrhythmia & Electrophysiology Review*, **4**(1), 40–43.

McDowell, K. S., Vadakkumpadan, F., Blake, R., Blauer, J., Plank, G., Macleod, R. S., & Trayanova, N. A. (2013). Mechanistic inquiry into the role of tissue remodeling in fibrotic lesions in human atrial fibrillation. *Biophysical Journal*, **104**(12), 2764–2773.

Molina, C. E., Abu-Taha, I. H., Wang, Q., Roselló-Díez, E., Kamler, M., Nattel, S., Ravens, U., Wehrens, X. H. T., Hove-Madsen, L., Heijman, J., & Dobrev, D. (2018). Profibrotic, electrical, and calcium-handling remodeling of the atria in heart failure patients with and without atrial fibrillation. *Frontiers in Physiology*, **9**, 1383.

Morgan, R., Colman, M. A., Chubb, H., Seemann, G., & Aslanidi, O. V. (2016). Slow conduction in the border zones of patchy fibrosis stabilizes the drivers for atrial fibrillation: Insights from multi-scale human atrial modeling. *Frontiers in Physiology*, **7**, 474.

Namekata, I., Tsuneoka, Y., Takahara, A., Shimada, H., Sugimoto, T., Takeda, K., Nagaharu, M., Shigenobu, K., Kawanishi, T., & Tanaka, H. (2009). Involvement of the $Na^+/Ca^{2+}$ exchanger in the automaticity of guinea-pig pulmonary vein myocardium as revealed by SEA0400. *Journal of Pharmacological Sciences*, **110**(1), 111–116.

Nattel, S., Burstein, B., & Dobrev, D. (2008). Atrial remodeling and atrial fibrillation. *Circulation: Arrhythmia and Electrophysiology*, **1**(1), 62–73.

Nattel, S., & Dobrev, D. (2012). The multidimensional role of calcium in atrial fibrillation pathophysiology: Mechanistic insights and therapeutic opportunities. *European Heart Journal*, **33**(15), 1870–1877.

Nattel, S., Guasch, E., Savelieva, I., Cosio, F. G., Valverde, I., Halperin, J. L., Conroy, J. M., Al-Khatib, S. M., Hess, P. L., Kirchhof, P., De Bono, J., Lip, G. Y. H., Banerjee, A., Ruskin, J., Blendea, D., & Camm, A. J. (2014). Early management of atrial fibrillation to prevent cardiovascular complications. *European Heart Journal*, **35**(22), 1448–1456.

Niederer, S. A., Lumens, J., & Trayanova, N. A. (2019). Computational models in cardiology. *Nature Reviews Cardiology*, **16**(2), 100–111.

Patterson, E., Lazzara, R., Szabo, B., Liu, H., Tang, D., Li, Y.-H., Scherlag, B. J., & Po, S. S. (2006). Sodium-calcium exchange initiated by the $Ca^{2+}$ transient: An arrhythmia trigger within pulmonary veins. *Journal of the American College of Cardiology*, **47**(6), 1196–1206.

Patterson, E., Po, S. S., Scherlag, B. J., & Lazzara, R. (2005). Triggered firing in pulmonary veins initiated by in vitro autonomic nerve stimulation. *Heart Rhythm*, **2**(6), 624–631.

Rietdorf, K., Bootman, M. D., & Sanderson, M. J. (2014). Spontaneous, pro-arrhythmic calcium signals disrupt electrical pacing in mouse pulmonary vein sleeve cells. *PLoS ONE*, **9**(2), e88649.

Roney, C. H., Bayer, J. D., Cochet, H., Meo, M., Dubois, R., Jaïs, P., & Vigmond, E. J. (2018). Variability in pulmonary vein electrophysiology and fibrosis determines arrhythmia susceptibility and dynamics. *PLoS Computational Biology*, **14**(5), e1006166.

Sanders, P., Berenfeld, O., Hocini, M., Jaïs, P., Vaidyanathan, R., Hsu, L.-F., Garrigue, S., Takahashi, Y., Rotter, M., Sacher, F., Scavée, C., Ploutz-Snyder, R., Jalife, J., & Haïssaguerre, M. (2005). Spectral analysis identifies sites of high-frequency activity maintaining atrial fibrillation in humans. *Circulation*, **112**(6), 789–797.

Schotten, U., Verheule, S., Kirchhof, P., & Goette, A. (2011). Pathophysiological mechanisms of atrial fibrillation: A translational appraisal. *Physiological Reviews*, **91**(1), 265–325.

Shiferaw, Y., Aistrup, G. L., & Wasserstrom, J. A. (2017). Mechanism for triggered waves in atrial myocytes. *Biophysical Journal*, **113**(3), 656–670.

Stewart, S., Murphy, N., Walker, A., McGuire, A., & McMurray, J. J. V. (2004). Cost of an emerging epidemic: An economic analysis of atrial fibrillation in the UK. *Heart*, **90**(3), 286–292.

Takahara, A., Hagiwara, M., Namekata, I., & Tanaka, H. (2014). Pulmonary vein myocardium as a possible pharmacological target for the treatment of atrial fibrillation. *Journal of Pharmacological Sciences*, **126**(1), 1–7.

Vagos, M., van Herck, I. G. M., Sundnes, J., Arevalo, H. J., Edwards, A. G., & Koivumäki, J. T. (2018). Computational modeling of electrophysiology and pharmacotherapy of atrial fibrillation: Recent advances and future challenges. *Frontiers in Physiology*, **9**, 1221.

Varela, M., Colman, M. A., Hancox, J. C., & Aslanidi, O. V. (2016). Atrial heterogeneity generates re-entrant substrate during atrial fibrillation and anti-arrhythmic drug action: Mechanistic insights from canine atrial models. *PLoS Computational Biology*, **12**(12), e1005245.

Varela, M., Morgan, R., Theron, A., Dillon-Murphy, D., Chubb, H., Whitaker, J., Henningsson, M., Aljabar, P., Schaeffter, T., Kolbitsch, C., & Aslanidi, O. V. (2017). Novel MRI technique enables non-invasive measurement of atrial wall thickness. *IEEE Transactions on Medical Imaging*, **36**(8), 1607–1614.

Varela, M., Roy, A., & Lee, J. (2021). A survey of pathways for mechano-electric coupling in the atria. *Progress in Biophysics and Molecular Biology*, **159**, 136–145.

Voigt, N., Heijman, J., Wang, Q., Chiang, D. Y., Li, N., Karck, M., Wehrens, X. H. T., Nattel, S., & Dobrev, D. (2014). Cellular and molecular mechanisms of atrial arrhythmogenesis in patients with paroxysmal atrial fibrillation. *Circulation*, **129**(2), 145–156.

Workman, A. J. (2010). Cardiac adrenergic control and atrial fibrillation. *Naunyn-Schmiedebergs Archives of Pharmacology*, **381**(3), 235–249.

Workman, A. J., Kane, K. A., & Rankin, A. C. (2001). The contribution of ionic currents to changes in refractoriness of human atrial myocytes associated with chronic atrial fibrillation. *Cardiovascular Research*, **52**(2), 226–235.

Xie, Y., Sato, D., Garfinkel, A., Qu, Z., & Weiss, J. N. (2010). So little source, so much sink: Requirements for after-depolarizations to propagate in tissue. *Biophysical Journal*, **99**(5), 1408–1415.

Yamashita, K., Silvernagel, J., Kwan, E., Kamali, R., Ghafoori, E., MacLeod, R., Dosdall, D. J., & Ranjan, R. (2019). Changes in atrial electrophysiological and structural substrate and their relationship to histology in a long-term chronic canine atrial fibrillation model. *Pacing and Clinical Electrophysiology*, **42**(7), 930–936.

## Additional information

### Data availability statement

Model code is available open-source, packaged with the Multi-scale cardiac Simulation Framework available at

https://zenodo.org/records/10606628 and can be cited using the "all versions DOI" https://doi.org/10.5281/zenodo.10204624. Tissue model reconstructions are available at: https://zenodo.org/records/10563535 and cited via: https://doi.org/10.5281/zenodo.10563534.

## Competing interests

No competing interests declared.

## Author contributions

M.C. and O.A. conceived and designed the study; M.C., M.V. and O.A. developed computational models; M.C. performed simulations and constructed illustrations; M.V., O.A., J.H. and R.M. acquired and processed experimental imaging data; all authors contributed to data analysis; M.C. drafted the manuscript, and all authors edited the manuscript. All authors have read and approved the final version of the manuscript. In addition, all authors agree to be accountable for all aspects of the work in ensuring that questions related to the accuracy or integrity of any part of the work are appropriately investigated and resolved. All persons designated as authors qualify for authorship, and all those that qualify for authorship are listed.

## Funding

This work was supported by a Medical Research Council, United Kingdom, Strategic Skills Fellowship (Grant Number MR/M014967/1) and Career Development Award (Grant Number MR/V010050/1) awarded to M.C., and by project grants from the British Heart Foundation, United Kingdom, awarded to M.V. (Grant Number RE/18/4/34215) and O.A. and J.H. (Grant Number PG/15/8/31130). Data acquisition and processing was supported by the National Institutes of Health (NIH) grants R01HL142923, and R24GM136986.

## Acknowledgements

This work was undertaken on ARC3 and ARC4, part of the High Performance Computing facilities at the University of Leeds, UK, and would not have been feasible without these facilities.

## Keywords

arrhythmia, atrial fibrillation, atrial remodelling, computational modelling, spontaneous triggers

## Supporting information

Additional supporting information can be found online in the Supporting Information section at the end of the HTML view of the article. Supporting information files available:

**Peer Review History**
**Text S1**
**Text S2**
**Video S1**
**Video S2**
**Video S3**